IRAQI JOURNAL OF MATERIALS
Volume (4) Issue (4) October-December 2025, pp. 153-162

Influence of FeO Layer Thickness on Characteristics of FeO/Porous Silicon Heterojunction Photodetectors

Jasim A. Yaseen

Department of Materials Engineering, College of Engineering, Thi Qar University, Nasiriyah, IRAQ

Abstract
This work investigates the influence of iron oxide (FeO) layer thickness on the optoelectronic performance of FeO/porous silicon (PSi) heterojunction photodetectors. Devices with FeO thicknesses of 100, 200, and 300 nm were fabricated and evaluated in terms of dark current, photocurrent, sensitivity, spectral responsivity, external quantum efficiency (EQE), specific detectivity (D^*), noise-equivalent power (NEP), and temporal response. The results reveal that the FeO thickness plays a decisive role in charge transport, carrier recombination, and optical absorption. A 200 nm FeO layer exhibited optimal behavior, achieving the highest responsivity (0.55 A/W at ~550 nm), EQE (~1.25%), and detectivity (~1.0×10^{13} Jones), along with the lowest NEP (~4×10^{-12} W). While thinner layers (100 nm) suffered from poor light absorption and incomplete passivation, thicker layers (300 nm) introduced higher series resistance and trap states, degrading performance. The findings demonstrate that precise control of FeO thickness is critical for optimizing FeO/PSi heterojunction photodetectors for visible light applications.

Keywords: Photodetectors; Heterojunctions; Iron oxide; Porous silicon
Received: 19 June 2025; **Revised:** 2 August 2025; **Accepted:** 9 August 2025; **Published:** 1 October 2025

1. Introduction

A photodetector is a fundamental optoelectronic device that converts incident light signals into measurable electrical signals. They are the cornerstone of modern technology, found in applications ranging from digital imaging and optical communications to environmental monitoring and biomedical sensing. The relentless pursuit of higher efficiency, faster response, broader spectral range, and lower cost has driven the development of advanced photodetector architectures, among which heterojunction devices are particularly prominent [1-3]. A heterojunction is an interface between two dissimilar semiconducting materials with different band gaps. This inherent asymmetry creates a built-in potential and band bending at the junction, which is highly advantageous for photodetection [4]. When a heterojunction photodetector is illuminated with photons of energy greater than the band gap of one or both semiconductors, electron-hole pairs (EHPs) are generated [5]. The internal electric field at the junction effectively separates these photogenerated carriers, sweeping electrons to one side and holes to the other, thereby generating a photocurrent without the need for an external bias in some cases (photovoltaic mode) [6].

The performance of a heterojunction photodetector is governed by the band alignment at the interface. The three primary types are Type-I (Straddling Gap), Type-II (Staggered Gap), and Type-III (Broken Gap) [7,8]. In the straddling gap, the band gap of one material lies entirely within the band gap of the other. This confines both electrons and holes to the same layer, favoring light emission (e.g., in LEDs) but is less ideal for detection due to higher recombination. In the staggered gap, the valence band and conduction band of one material are both higher than those of the other. This spatial separation of electrons and holes into different materials drastically reduces recombination, making it highly efficient for photodetection and photovoltaic applications. In the broken gap, there is an overlap between the valence band of one material and the conduction band of the other. This creates a tunneling junction, useful for high-speed devices [9-11]. The integration of nanostructured materials like porous silicon (PSi) with functional nanoparticles like iron oxide (FeO) creates a complex heterojunction system that can be engineered to excel across these metrics [12]. Porous silicon is a nanostructured form of silicon characterized by a sponge-like network of pores and silicon nanocrystals. Since the discovery of its efficient visible photoluminescence at room temperature in 1990, it has evolved from a laboratory curiosity into a versatile platform for optoelectronics, sensing, and biomedicine [13-16].

The most common and controllable method for producing PSi is electrochemical etching of a single-crystal silicon wafer in a hydrofluoric (HF) acid-based electrolyte. The basic setup consists of a Teflon

cell where the Si wafer (anode) and a platinum cathode are immersed in the HF solution. Upon applying a current, the following reactions occur at the silicon surface [17]:
Anode (Si): $Si + 2HF + 2h^+ \rightarrow SiF_2 + 2H^+ \mid SiF_2 + 2HF \rightarrow SiF_4 + H_2 \mid SiF_4 + 2HF \rightarrow H_2SiF_6$
Cathode (Pt): $2H^+ + 2e^- \rightarrow H_2(g)$

The holes (h^+) required for the dissolution reaction are supplied by the current. The key to porosity is the preferential etching of silicon at the pore tips, while the hydrogen passivation of the silicon skeleton walls prevents lateral etching.

The morphology of PSi - including porosity (percentage of void volume), pore size (from microporous <2 nm to macroporous >50 nm), layer thickness, and nanocrystal size - is not fixed but can be precisely engineered by controlling the etching parameters: current density, HF concentration, etching time, silicon doping type and level, and illumination. Higher current densities generally lead to higher porosity and larger pore sizes. Lower HF concentrations favor the formation of larger pores. Etching time directly controls the thickness of the porous layer [18-20]. The p-type silicon typically produces finer, more branched pores compared to n-type under similar conditions. For n-type Si, light illumination is crucial to generate the necessary holes for the etching process. This tunability allows PSi to be fabricated as single layers, multi-layers, microcavities, and even photonic crystals with precisely designed optical properties, such as photonic band gaps [21-23].

Porous silicon (PSi) can have an enormous internal surface area, up to 500 m^2/cm^3. This makes it an exceptional host matrix for infiltrating nanoparticles, dyes, or biomolecules, amplifying any surface-related interactions [24]. The effective refractive index of a PSi layer is a weighted average of air (n=1) and silicon (n~3.5). By varying the porosity, the refractive index can be tuned. This enables the design of optical interference structures like Bragg reflectors and optical microcavities that can enhance light-matter interaction within the layer [25]. Due to quantum confinement effects, silicon nanocrystals in the PSi matrix can emit light in the visible range, a property not found in bulk silicon. The freshly etched PSi surface is hydride-terminated ($Si-H_x$), which is relatively unstable. It can be easily oxidized or functionalized with organic monolayers (e.g., silanization) to improve stability and attach specific receptor molecules for sensing applications. This active surface is ideal for the subsequent deposition of iron oxide nanoparticles [26].

The formation of a high-quality heterojunction is critical. The chosen method determines the uniformity, adhesion, and interfacial contact between the FeO nanoparticles and the complex 3D structure of the PSi. Drop casting and spin coating are the simplest methods. A colloidal suspension of pre-synthesized iron oxide nanoparticles (often stabilized by surfactants) is prepared in a suitable solvent. In drop casting, a droplet of the suspension is directly applied onto the PSi surface and allowed to dry slowly [27,28]. Capillary forces draw the nanoparticles into the pores. In spin coating, the PSi substrate is spun at high speed (e.g., 1000-3000 rpm), and the nanoparticle suspension is dropped onto it [29]. Centrifugal force spreads the solution evenly and drives it into the pores [30]. These methods exhibit advantages such as simplicity, low cost, no need for complex equipment, while they include disadvantages such as poor control over penetration depth and distribution within the pores; aggregation of nanoparticles can occur upon drying; the surfactant shell can act as an insulating barrier, hindering electrical transport at the heterojunction [31].

Thermal evaporation and annealing is a vacuum deposition technique and commonly used for thin films. In this method, high-purity iron is heated in a vacuum chamber until it evaporates. The vapor condenses as a thin metallic Fe film on the surface and, to a lesser extent, within the top layers of the PSi pores. The sample is then subjected to a thermal annealing process in a controlled atmosphere (e.g., oxygen for Fe_2O_3, or a slight vacuum for Fe_3O_4) to fully oxidize the iron film into nanoparticles [32,33]. The advantages are high purity of the deposited material; good control over the total amount of Fe deposited. The disadvantages are limited penetration into deep pores, often resulting in a capping layer on top of the PSi rather than a truly infiltrated nanocomposite; requires expensive vacuum equipment [34].

Chemical bath deposition (CBD) is a low-temperature, solution-based method akin to electrodes plating. In this method, the PSi sample is immersed in an aqueous solution containing an iron salt (precursor) and a complexing agent (e.g., EDTA). The solution is heated, which causes the slow release of Fe ions and their hydrolysis, leading to the controlled precipitation of iron oxide on the internal surfaces of the PSi. The reaction relies on the adsorption of species onto the substrate [35]. As advantages, this method is simple, low-cost, scalable; can achieve good pore filling and uniformity, while as disadvantages, this method can be slow; control over the crystallinity and stoichiometry of the deposited oxide can be challenging; may require post-deposition annealing [36].

Studies have shown that fabricated FeO/PSi heterostructures can exhibit significantly higher

 ISSN (print) 2958-8960 (online) 3006-6042 Printed in IRAQ

photoresponse (responsivity and EQE) under visible light illumination compared to bare PSi-based devices, validating the effectiveness of this nanocomposite approach. FeO/PSi heterojunction photodetectors extend beyond simple light sensing. Their unique properties make them suitable for biomedical sensing as the high surface area and tunable porosity make PSi an ideal transducer. Functionalizing the FeO/PSi structure with specific antibodies or DNA strands can create label-free photonic biosensors where the binding of a target analyte causes a measurable shift in the photocurrent [37,38]. In photoelectrochemical (PEC) sensing, these devices can operate in a PEC cell configuration for detecting species in solution. The photocurrent generated under light is highly sensitive to surface reactions, enabling the detection of pollutants, biomarkers, or glucose. Low-cost and flexible optoelectronics employ both PSi (through etching of thin Si wafers) and FeO are low-cost materials. Strategies to create flexible PSi membranes could pave the way for flexible photodetectors [39]. The future of this field lies in achieving even greater control over the material properties. This includes precise engineering of the band gap of PSi nanocrystals, synthesizing FeO nanoparticles with tailored shapes and crystal facets to optimize charge transfer, and developing novel deposition techniques that ensure perfect, uniform coating of the complex PSi nanostructure without pore blocking [40-42].

2. Experimental Work

High-purity FeO thin films were fabricated on glass substrates via chemical bath deposition. A 99.99% pure iron precursor supplied by Chemical Base (India) was employed as the source of iron ions. The oxygen was pumped into the solution at 10 L/min flow rate. The photo-electrochemical etching was used to generate porous silicon (PSi) layers on p-type silicon wafers. The wafers were diced into 2.25 cm² pieces, thoroughly rinsed with ethanol and deionized water, and immersed for ten minutes in an HF–ethanol solution (1:20 v/v) for surface cleaning. Prior to etching, the substrates were again rinsed with deionized water and ethanol. Etching was conducted in a photo-electrochemical cell filled with a 1:10 HF–ethanol mixture, under a constant DC current of 20 mA for 20 minutes. Following etching, the samples were immediately transferred to methanol to minimize oxidation and airborne contamination.

For device preparation, FeO nanopowder was dispersed in deionized water to form aqueous suspensions of 10^{-4}-10^{-3} g/mL by dissolving powder (1, 2, and 3 mg) in 2 mL of solvent. Each suspension was sonicated for 30 minutes to achieve uniform dispersion of nanoparticles. Using a micropipette, controlled volumes of the prepared colloids were deposited dropwise onto the porous silicon layers. After each drop, the samples were placed on a hotplate at 40 °C for one minute to ensure proper adhesion and drying. This deposition cycle was repeated six times to ensure sufficient nanoparticle loading across the porous surface. Figure (1) shows a scheme of the FeO/PSi heterostructures fabricated in this work.

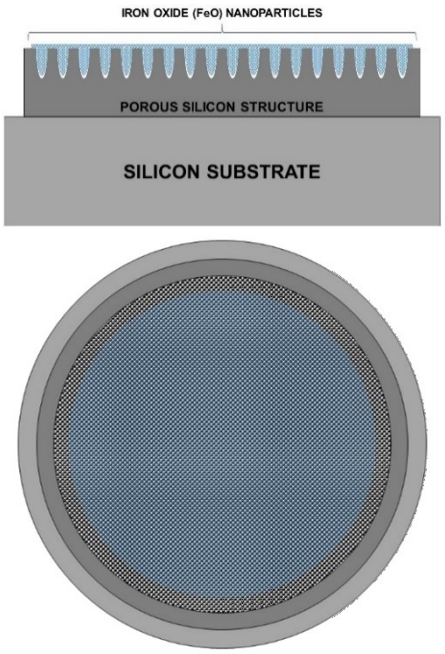

Fig. (1) Scheme of the FeO/PSi heterostructures fabricated in this work

3. Results and Discussion

Figure (2) illustrates the relationship between forward current and applied voltage for FeO/PSi structures with varying FeO layer thicknesses. The data shows that as the thickness of the FeO layer increases from 100 nm to 300 nm, the forward current also increases significantly for the same applied voltage. At a voltage of 10 V, for example, the device with the 300 nm FeO layer reaches a current of approximately 250 mA, while the 100 nm layer only reaches about 150 mA. This indicates that the thicker FeO layer provides improved charge transport, likely due to a lower overall series resistance. The FeO layer acts as a passivation and protection layer and its thickness can influence the resistance and electrical transport properties of the overall structure. A thicker, well-formed FeO layer might lead to better contact with the porous silicon (PSi) and the metal electrode, reducing interface resistance. The nonlinear, curved relationship between current and voltage suggests that the electrical transport is not purely ohmic and may be governed by a mechanism like space-charge-limited current or Poole-Frenkel emission, which is common in semiconductor heterojunctions.

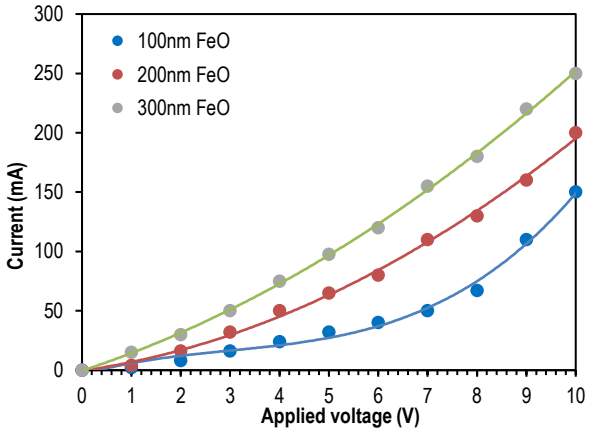

Fig. (2) Variation of forward dark current of the FeO/PSi heterostructure with applied voltage for three different thicknesses of FeO layer

Figure (3) illustrates the reverse dark current as a function of applied voltage for FeO/PSi structures with varying FeO layer thicknesses. The data shows that the reverse current increases nonlinearly with increasing negative voltage, which is characteristic of leakage current in a diode structure. A notable observation is that as the FeO layer thickness increases, the reverse current also increases slightly, which is counterintuitive for an ideal heterojunction where a thicker layer might provide better insulation. For example, at -10 V, the device with the 300 nm FeO layer has a current of approximately -6.0 mA, which is marginally higher than the 100 nm layer's current of about -5.5 mA. This suggests that the thicker layer, while providing better forward conduction, may also introduce more defects or trap states that contribute to the reverse leakage current. These defects could create pathways for current flow under reverse bias, which is a key performance limitation for semiconductor devices.

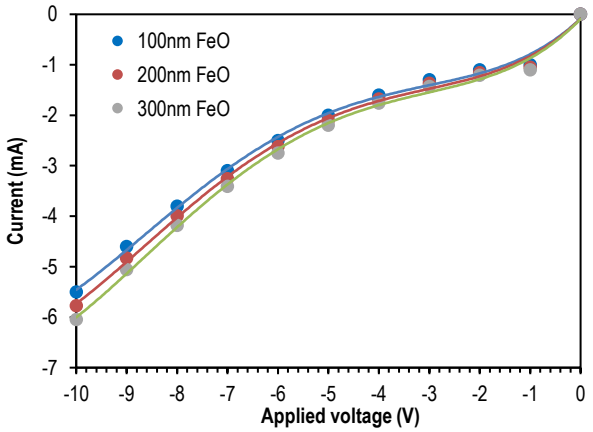

Fig. (3) Variation of reverse dark current of the FeO/PSi heterostructure with applied voltage for three different thicknesses of FeO layer

Figure (4) shows the reverse photocurrent as a function of applied voltage for FeO/PSi structures under a light intensity of 120 W/cm². A clear trend emerges: as the applied voltage becomes more negative, the reverse photocurrent increases significantly. This is typical behavior for a photodetector, as the reverse bias widens the depletion region, which improves the collection efficiency of photogenerated electron-hole pairs. This figure also highlights a strong dependence on the thickness of the FeO layer. At any given voltage, the photocurrent increases with the thickness of the FeO layer, reaching its highest value of approximately -8.0 mA at -10 V for the 300 nm sample. This suggests that a thicker FeO layer, in this illuminated state, is more effective at generating and/or collecting charge carriers. This could be due to a more extensive absorption of light within the thicker layer or an improved interface with the porous silicon, leading to better charge separation and transport under illumination.

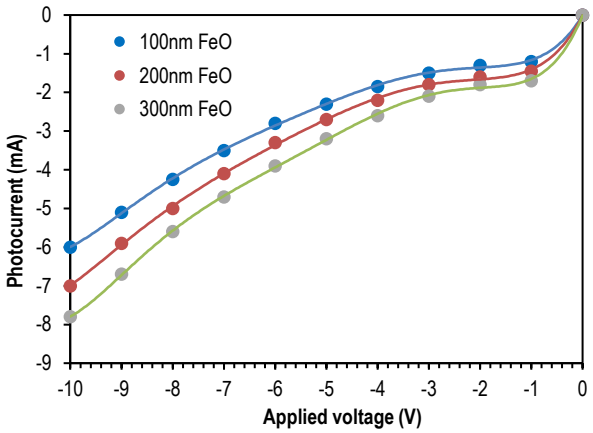

Fig. (4) Variation of photocurrent of the FeO/PSi heterostructure with applied reverse voltage for three different thicknesses of FeO layer

Figure (5) presents the sensitivity of FeO/PSi photodetectors as a function of reverse applied voltage, for different FeO layer thicknesses, under a light intensity of 120 W/cm². The data clearly shows a linear increase in sensitivity with increasing reverse voltage for all samples. This behavior is expected, as a higher reverse bias increases the electric field across the device, which in turn improves the efficiency of collecting photogenerated charge carriers, leading to a stronger photocurrent response relative to the dark current. Furthermore, this figure demonstrates a strong positive correlation between sensitivity and FeO layer thickness. The device with the 300 nm FeO layer consistently exhibits the highest sensitivity, reaching nearly 155% at -10 V. In contrast, the 100 nm FeO layer device has the lowest sensitivity, peaking at around 120% at the same voltage. The thicker FeO layer likely offers a larger volume for light absorption and subsequent electron-hole pair generation, contributing to a more significant photocurrent and a higher sensitivity. This confirms that the thickness of the FeO layer is a critical parameter for optimizing the performance of these photodetector structures.

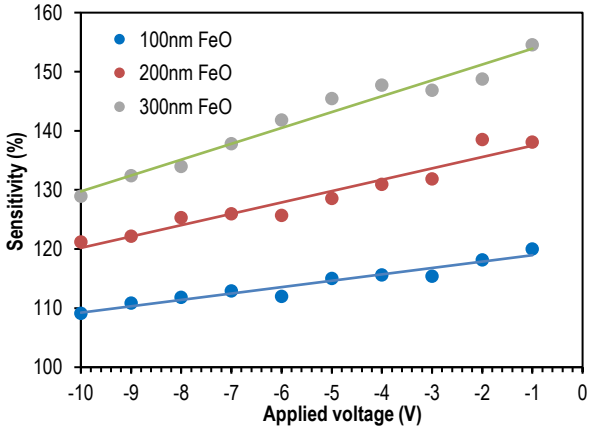

Fig. (5) Variation of sensitivity of the FeO/PSi heterostructure with applied voltage for three different thicknesses of FeO layer

Figure (6) illustrates the spectral responsivity of FeO/PSi photodetectors as a function of wavelength, highlighting how the thickness of the FeO layer influences performance. Spectral responsivity, measured in Amperes per Watt (A/W), indicates how efficiently a device converts incident light into electrical current at a specific wavelength. A higher responsivity value signifies better light detection at that wavelength. The data reveals that all three devices, regardless of FeO thickness, exhibit a bell-shaped responsivity curve, with a peak responsivity in the visible spectrum. The responsivity begins to rise at approximately 450 nm, peaks in the green-yellow region, and then gradually decreases into the near-infrared. This suggests that the devices are most sensitive to visible light, which is consistent with the bandgap properties of the constituent materials, particularly porous silicon (PSi). A key finding is the significant impact of the FeO layer thickness on the magnitude of the responsivity. The device with the 200 nm FeO layer consistently shows the highest responsivity, peaking at approximately 0.55 A/W near 550 nm. In contrast, the 300 nm FeO layer device has a lower peak responsivity of about 0.3 A/W, and the 100 nm FeO layer device is the least sensitive, with a peak of only 0.2 A/W. This finding is crucial and suggests an optimal FeO thickness for light absorption and charge collection. A 100 nm layer is likely too thin to effectively absorb incoming photons and fully passivate the porous silicon, leading to low responsivity. Conversely, while the 300 nm layer may absorb more light, its increased thickness could also lead to higher series resistance and increased recombination losses, trapping photogenerated carriers before they can contribute to the photocurrent. The 200 nm thickness appears to be the sweet spot, providing an ideal balance between light absorption, reduced recombination, and efficient charge transport, leading to the highest responsivity.

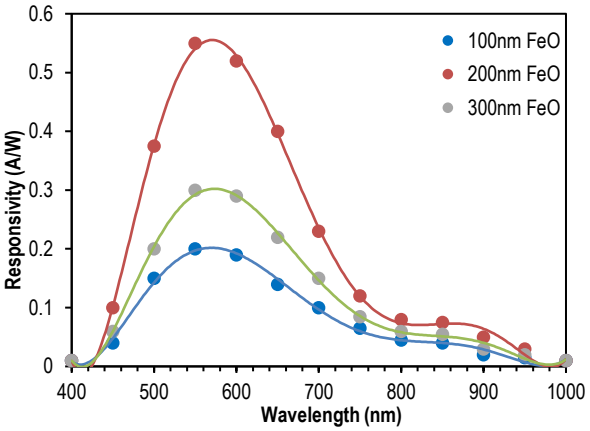

Fig. (6) Variation of spectral responsivity of the FeO/PSi heterostructure as function of incident wavelength for three different thicknesses of FeO layer

Figure (7) displays the external quantum efficiency (EQE) as a function of wavelength for FeO/PSi photodetectors with different FeO layer thicknesses. EQE, expressed as a percentage, represents the ratio of the number of charge carriers collected by the device to the number of incident photons. It is a critical metric for evaluating a photodetector's performance, as it quantifies the combined effect of light absorption, carrier generation, and charge collection efficiency. This figure reveals that all three devices exhibit a similar spectral response profile, with a broad peak in the visible light range (450–700 nm) and a sharp decline at shorter wavelengths, indicating a cutoff around the bandgap of the materials. This suggests that the devices are most effective at converting visible light into an electrical signal. A key finding is the dramatic influence of the FeO layer thickness on the magnitude of the EQE. The device with the 200 nm FeO layer consistently demonstrates the highest EQE, peaking at approximately 1.25% at a wavelength of around 550 nm. This is a significant improvement over the other two devices. The 300 nm FeO layer device has a lower peak EQE of about 0.65%, while the 100 nm FeO layer device is the least efficient, with a peak EQE of only about 0.45%. This trend suggests that there is an optimal thickness for the FeO layer that maximizes the photodetector's efficiency. A 100 nm layer is likely too thin to fully absorb incident photons and passivate the porous silicon, leading to low quantum efficiency. Conversely, while a thicker 300 nm layer may absorb more light, it could also increase the series resistance and recombination rate of photogenerated carriers. This would lead to a lower EQE, as more carriers are lost before they can be collected. The 200 nm thickness appears to strike the best balance, maximizing light absorption while minimizing carrier losses, thus achieving the highest external quantum efficiency.

ISSN (print) 2958-8960 (online) 3006-6042 Printed in IRAQ

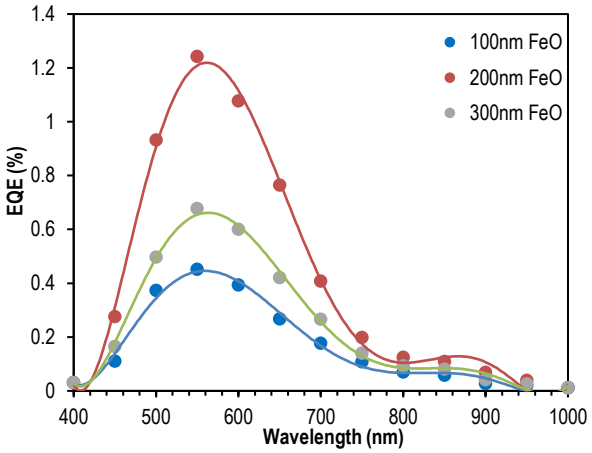

Fig. (7) Variation of external quantum efficiency (EQE) of the FeO/PSi heterostructure as function of incident wavelength for three different thicknesses of FeO layer

Figure (8) illustrates the specific detectivity (D∗) as a function of wavelength for FeO/PSi photodetectors with different FeO layer thicknesses. Specific detectivity is a normalized figure of merit used to compare the performance of photodetectors, independent of their area and bandwidth. A higher D∗ value indicates a better ability to detect very faint light signals, as it signifies a superior signal-to-noise ratio. This figure reveals a clear spectral response, with all devices exhibiting a broad peak in the visible light range, specifically between 500 nm and 600 nm. This is consistent with the spectral responsivity and quantum efficiency plots, confirming that these FeO/PSi devices are optimized for detecting visible light. A key finding from this data is the strong dependence of specific detectivity on the FeO layer thickness. The device with the 200 nm FeO layer shows the highest specific detectivity, peaking at a remarkable value of approximately 10×10^{13} Jones. This significantly outperforms both the 300 nm FeO layer device, which peaks at about 5.5×10^{13} Jones, and the 100 nm FeO layer device, which has the lowest peak detectivity at approximately 3.5×10^{13} Jones. This trend underscores the presence of an optimal thickness for the FeO layer. While a thicker FeO layer (300 nm) might absorb more light, it also likely increases noise current from defects and recombination centers, which would reduce the signal-to-noise ratio and, consequently, the specific detectivity. Conversely, a very thin FeO layer (100 nm) may not provide sufficient light absorption or effective passivation of the porous silicon, leading to lower signal generation and thus, a lower specific detectivity. The 200 nm thickness represents a critical balance where light absorption and carrier generation are maximized while noise-contributing factors are minimized, resulting in the highest overall photodetector performance.

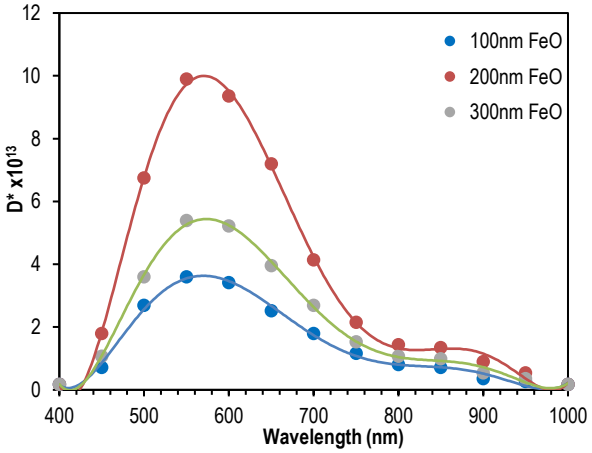

Fig. (8) Variation of specific detectivity (D*) of the FeO/PSi heterostructure as function of incident wavelength for three different thicknesses of FeO layer

Figure (9) illustrates the noise equivalent power (NEP) as a function of wavelength for FeO/PSi photodetectors with different FeO layer thicknesses. NEP is a fundamental metric for assessing the

ISSN (print) 2958-8960 (online) 3006-6042 Printed in IRAQ

performance of a photodetector. It represents the minimum optical power required for the signal-to-noise ratio to equal one. In simpler terms, a lower NEP value indicates a more sensitive device that can detect weaker light signals. This figure shows that all three devices exhibit a similar spectral profile, with the NEP value being at its lowest in the visible light range (approximately 500 nm to 600 nm). This corresponds to the wavelengths where the photodetectors are most sensitive and have the highest responsivity, as seen in previous plots. As the wavelength moves away from this optimal range, towards both the ultraviolet and the near-infrared, the NEP increases sharply, indicating a decrease in device sensitivity. A key finding is the significant influence of the FeO layer thickness on the magnitude of the NEP. The device with the 200 nm FeO layer consistently exhibits the lowest NEP across the entire spectrum, reaching a minimum value of approximately 4×10^{-12} W. In contrast, the 100 nm FeO layer device has the highest NEP, while the 300 nm FeO layer device has an NEP between the other two. This trend is directly related to the device's overall performance. A lower NEP is a consequence of a high signal-to-noise ratio, which is achieved through a combination of high responsivity and low noise. The 200 nm FeO layer seems to provide the optimal balance between these factors, maximizing the signal generated from incident light while minimizing sources of noise, such as dark current and recombination. The higher NEP of the 100 nm and 300 nm devices suggests that they are less effective at this balance, either due to insufficient light absorption (100 nm) or increased noise-contributing defects (300 nm). This plot confirms that the 200 nm thickness is the most effective for achieving high-performance FeO/PSi photodetectors.

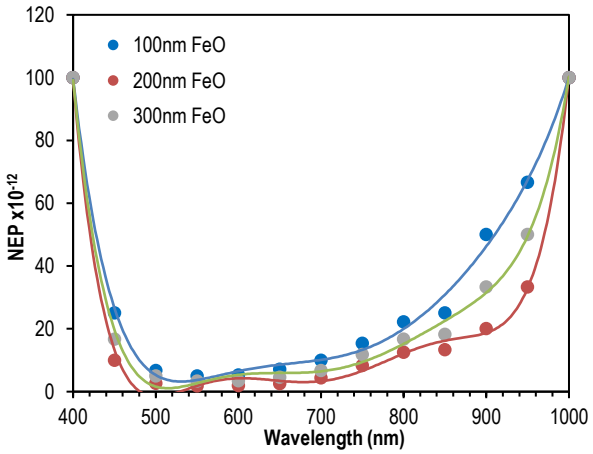

Fig. (9) Variation of NEP of the FeO/PSi heterostructure as function of incident wavelength for three different thicknesses of FeO layer

Figure (10) illustrates the temporal photo-response of FeO/PSi structures with different FeO layer thicknesses, measured as current versus time. The plot shows the devices' response to a pulsed light source, which is turned on and off at regular intervals. The photo-response behavior is critical for understanding a photodetector's speed, stability, and reliability. This figure shows a clear and repeatable cycling behavior for all three devices. When the light is turned on, the current instantaneously drops to a more negative value (relative to the dark current baseline), and when the light is turned off, the current returns to its baseline. The consistency of this square-wave-like response over time, with no discernible degradation, indicates that the devices are stable and reliable under repeated illumination cycles. This is a crucial characteristic for practical photodetector applications. The magnitude of the photo-response is directly related to the photocurrent generated. The plot shows a significant dependence on the FeO layer thickness, which confirms previous observations from the responsivity and quantum efficiency plots. The device with the 200 nm FeO layer exhibits the largest photo-response, with a substantial change in current from the dark to the illuminated state. The 300 nm FeO layer device has a smaller response, and the 100 nm FeO layer device shows the smallest change in current. This pattern confirms that there is an optimal thickness for the FeO layer that maximizes the photodetector's performance. The 200 nm thickness appears to be the most effective for several reasons:

- The 200 nm thickness likely provides an ideal volume for light absorption without introducing significant bulk resistance or recombination centers that would hinder charge transport. This allows for a higher number of photogenerated carriers to be collected, resulting in a stronger photo-response.

ISSN (print) 2958-8960 (online) 3006-6042 Printed in IRAQ

- An optimal FeO thickness may also lead to a better quality heterojunction with the porous silicon. A well-formed interface minimizes surface defects and trap states that can capture photogenerated carriers, thus allowing them to contribute to the photocurrent more effectively.
- The smaller photo-response of the 100 nm device suggests that it is too thin to absorb a sufficient number of photons. Conversely, the 300 nm device, despite being thicker, does not produce a higher current, likely due to increased series resistance or a higher density of defects that act as recombination centers.

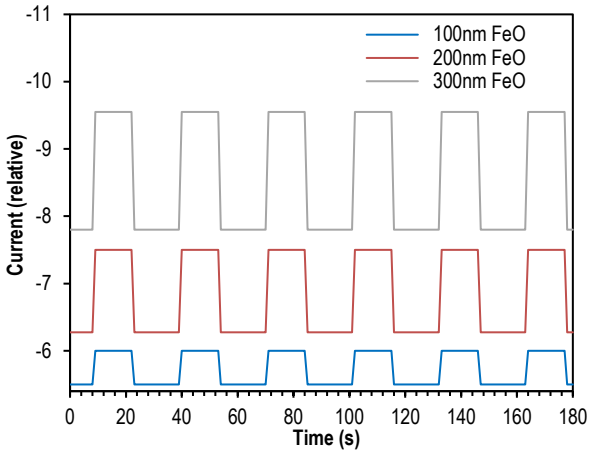

Fig. (10) Time-dependent behavior of current of the FeO/PSi heterostructure for three different thicknesses of FeO layer

4. Conclusions

The study confirms that FeO layer thickness strongly influences the optoelectronic characteristics of FeO/PSi heterojunction photodetectors. Among the tested devices, the 200 nm FeO layer offered the best balance between light absorption, carrier collection, and minimized recombination, leading to superior responsivity, quantum efficiency, and detectivity with the lowest NEP. Thinner layers lacked effective absorption, whereas thicker layers increased resistance and leakage pathways. The results highlight the importance of optimizing FeO thickness for high-performance photodetectors, establishing 200 nm as the most favorable condition in this study. These insights provide useful guidelines for designing cost-effective, visible-range optoelectronic devices.

References

[1] A.D.A. Bin Abu Sofian et al., “Upcycling and recycling of spent battery waste for a sustainable future: Progress and perspectives”, *Prog. Mater. Sci.*, 153 (2025) 101478.
[2] J. Li, Q. Cai, and B.A. Horri, “Highly conductive and stable electrolytes for solid oxide electrolysis and fuel cells: fabrication, characterisation, recent progress and challenges”, *Mater. Adv.*, 6(1) (2024) 39-83.
[3] P. Zhang et al., “Ordered mesoporous materials for water pollution treatment: Adsorption and catalysis”, *Green Ener. Enviro.*, 9(8) (2024) 1239-1256.
[4] X. Shang et al., “A molecular view of single-atom catalysis toward carbon dioxide conversion”, *Chem. Sci.*, 15(13) (2024) 4631-4708.
[5] X. Liu et al., “Solid-state mechanochemistry advancing two dimensional materials for lithium-ion storage applications: A mini review”, *Nano Mater. Sci.*, 5(2) (2023) 210-227.
[6] M. Ma et al., “Electrode particulate materials for advanced rechargeable batteries: A review”, *Particuol.*, 86 (2024) 160-181.
[7] A.F.H. Kaplan, T. Fedina, and F. Brueckner, “Study of Si-domains enabling local reduction of laser-melted iron ore for iron-making during 3D-printing”, *Procedia CIRP*, 111 (2022) 377-380.
[8] M. Muddasar, M. Culebras, and M.N. Collins, “Lignin and its carbon derivatives: Synthesis techniques and their energy storage applications”, *Mater. Today Sustain.*, 28 (2024) 100990.
[9] M. Arif et al., “Photo-assisted Li/Zn-air batteries and supercapacitors: material design, working mechanism and challenges”, *Adv. Powder Mater.*, 4(5) (2025) 100316.
[10] X. Chen et al., “Towards removal of PPCPs by advanced oxidation processes: A review”, *Results Eng.*, 20 (2023) 101496.
[11] Z. Wang et al., “A review of designable deep eutectic solvents for green fabrication of advanced functional materials”, *RSC Sustain.*, 3(2) (2025) 738-756.
[12] S. Foorginezhad et al., “Review and analysis of porous adsorbents for effective CO_2 capture”, *Renew. Sustain. Ener. Rev.*, 215 (2025) 115589.
[13] N.K. Chowdhury and B. Bhowmik, “Micro/nanostructured gas sensors: the physics behind the nanostructure growth, sensing and selectivity mechanisms”, *Nanoscale Adv.*, 3(1) (2021) 73-93.
[14] M. Mushtaq, P. Uma Sathyakam and R. Vijayaraghavan, “Performance, comprehension and applications of hematite-based photoanodes in PEC water splitting”, *Next Mater.*, 3 (2024) 100159.
[15] F.B. Mohammed Ameen, G.G. Ali, and M.H. Younus, “Fabrication and Characterization of Gas Sensors from ZnS/Porous Silicon Heterojunctions”, *Iraqi J. Appl. Phys.,* 20(2B) (2024) 321-332.

 ISSN (print) 2958-8960 (online) 3006-6042 Printed in IRAQ

[16] A.T. Zakar, Z.T. AbdulRahman, and T.A. Zaker, "Study of Transient Laser-Induced Self-Focusing and Optical Modulation of Porous Silicon Films Using Pump-Probe Spectroscopy", *Iraqi J. Appl. Phys.,* 20(4) (2024) 867-872.
[17] J. Fu et al., "Fight for carbon neutrality with state-of-the-art negative carbon emission technologies", *Eco-Enviro. Health*, 1(4) (2022) 259-279.
[18] A.G. Díez et al., "Multicomponent magnetic nanoparticle engineering: the role of structure-property relationship in advanced applications", *Mater. Today Chem.*, 26 (2022) 101220.
[19] I.J. The et al., "Engineering high-performance $BiVO_4$ homo- and heterojunction Photoanodes for solar-driven Photoelectrochemical water splitting applications", *Coord. Chem. Rev.*, 541 (2025) 216773.
[20] A.T. Zakar, H.N. Mohammed, and T.A. Zaker, "Evaluation of Transient Thermoreflectance of Porous Silicon Membranes for Thermal Interface Applications", *Iraqi J. Appl. Phys.,* 20(2A) (2024) 215-220.
[21] W.A. Ali, S.E. Richards, and R.H. Alzard, "Unlocking the potential of ball milling for nanomaterial Synthesis: An overview", *J. Indust. Eng. Chem.*, 149 (2025) 63-93.
[22] S. Gao et al., "Research on the application of defect engineering in the field of environmental catalysis", *Green Ener. Enviro.*, 10(6) (2025) 1187-1209.
[23] L.H. Razzak, "Current-Voltage Characteristics of Silicon Nitride Nanoparticles Embedded in Porous Silicon Matrix", *Iraqi J. Appl. Phys. Lett.,* 7(3) (2024) 11-14.
[24] K.T. Alao et al., "Potential uses of perovskite-based photovoltaics for hydrogen production: A pathway to sustainable energy solutions", *Next Energy*, 7 (2025) 100215.
[25] W. Tang et al., "Recent advances of bifunctional catalysts for zinc air batteries with stability considerations: from selecting materials to reconstruction", *Nanoscale Adv.*, 5(17) (2023) 4368-4401.
[26] A. Jetybayeva et al., "Towards Li–S microbatteries: A perspective review", *J. Power Sources*, 573 (2023) 233158.
[27] M.R. Sonawane et al., "Adsorption of MO dyes using various adsorbents: Past, present and future perspective", *Next Sustain.*, 6 (2025) 100153.
[28] S. Saleem et al., "Analysis and characterization of opto-electronic properties of iron oxide (Fe_2O_3) with transition metals (Co, Ni) for the use in the photodetector application", *J. Mater. Res. Technol.*, 25 (2023) 6150-6166.
[29] Y. Naciri, M.N. Ghazzal, and E. Paineau, "Nanosized tubular clay minerals as inorganic nanoreactors for energy and environmental applications: A review to fill current knowledge gaps", *Adv. Colloid Interface Sci.*, 326 (2024) 103139.
[30] A. Nyabadza et al., "A review of physical, chemical and biological synthesis methods of bimetallic nanoparticles and applications in sensing, water treatment, biomedicine, catalysis and hydrogen storage", *Adv. Colloid Interface Sci.*, 321 (2023) 103010.
[31] Munir et al., "Benchmarking stable Electrocatalysts for green hydrogen production: A chemist perspective", *Coord. Chem. Rev.*, 521 (2024) 216112.
[32] T.-W. Chen et al., "An overview of semiconductor electrode materials for photoelectrochemical water splitting and CO_2 conversion", *Int. J. Electrochem. Sci.*, 19(5) (2024) 100542.
[33] S. Yu et al., "Recent development of catalytic strategies for sustainable ammonia production", *Chinese J. Chem. Eng.*, 62 (2023) 65-113.
[34] A. Nyabadza et al., "Advanced nanomaterials and dendrimers in water treatment and the recycling of nanomaterials: A review", *J. Enviro. Chem. Eng.*, 12(3) (2024) 112643.
[35] W.C. Ng et al., "Elevating the prospects of green hydrogen (H_2) production through solar-powered water splitting devices: A systematic review", *Sustain. Mater. Technol.*, 40 (2024) e00972.
[36] S. Shiva Kumar and H. Lim, "An overview of water electrolysis technologies for green hydrogen production", *Energy Rep.*, 8 (2022) 13793-13813.
[37] A. Schmid, L. Enzlberger, and J. Fleig, "Mechanistic insights into photo-current enhancement in photo-active $SrTiO_3$ heterojunctions under UV illumination", *Solid State Ionics*, 406 (2024) 116469.
[38] M. Morgenbesser et al., "$SrTiO_3$ based high temperature solid oxide solar cells: Photovoltages, photocurrents and mechanistic insight", *Solid State Ionics*, 368 (2021) 115700.
[39] M. Bulla et al., "Exploring the frontiers of carbon nanotube synthesis techniques and their potential applications in supercapacitors, gas sensing, and water purification", *J. Enviro. Chem. Eng.*, 12(6) (2024) 114504.
[40] N. Han et al., "Rational design of boron nitride with different dimensionalities for sustainable applications", *Renew. Sustain. Energy Rev.*, 170 (2022) 112910.
[41] M. Zheng et al., "Review on the synergistic effect of adsorption and photocatalytic degradation of patulin by functionalized graphitic carbon nitride nanomaterials and hydrogels", *RSC Adv.*, 15(30) (2025) 24510-24535.
[42] C.B. Nascimento et al., "Electronic properties of the passive films formed on CoCrFeNi and CoCrFeNiAl high entropy alloys in sodium chloride solution", *J. Mater. Res. Technol.*, 9(6) (2020) 13879-13892.

